Supporting information

Restricting the over-oxidation of active sites in high-entropy electrocatalysts towards ultra-stabilized oxygen evolution in alkaline electrolytic water

*Yimin Zhang,[a, b] Jianli Kang,[a, b] * Haonan Xie,[a, b] Hongxia Yin,[c] Zhijia Zhang,[d] Yuhan Ma,[e] Guangxin Sun,[e] Enzuo Liu,[a, b] Liying Ma,[a, b] Biao Chen,[a, b] Junwei Sha,[a, b] Lihua Qian,[c] Wenbin Hu,[a] Chunnian He,[a, b, d] Naiqin Zhao[a, b] **

a School of Materials Science and Engineering, Tianjin University, Tianjin, 300350, P.R. China.

b National Industry-Education Platform of Energy Storage, Tianjin University, 135 Yaguan Road, Tianjin 300350, People's Republic of China

c School of Physics, Huazhong University of Science and Technology, Wuhan 430074, P.R. China.

d School of Materials Science and Engineering, Tiangong University, Tianjin, 300387, P.R. China.

e Joint School of National University of Singapore and Tianjin University International Campus of Tianjin University, Binhai New City, Fuzhou 350207, P. R. China

Corresponding Author:

*Dr. Jianli Kang, E-mail: jianlikang@tju.edu.cn;

**Dr. Naiqin Zhao, E-mail: nqzhao@tju.edu.cn

1. Theoretical Calculations

All simulations were performed by the use of DFT which was implemented in the Vienna Ab-initio Simulation Package (VASP). The exchange-correlation was approximated using the generalized gradient approximation (GGA) with Perdew-Burke-Ernzerhof (PBE) functional. The atomic positions were optimized using the kinetic energy cutoff of 450 eV in the plane-wave expansion. Electron-ion interaction was described by the projector augmented wave (PAW) method. DFT-D2 method was applied to account for Van der Waals interaction.

For the AEM pathway in an alkaline electrolyte, the four-electron reactions are:

$$* + OH^- \rightarrow *OH + e^-, \quad (1)$$

$$*OH + OH^- \rightarrow *O + H_2O\ (l) + e^-, \quad (2)$$

$$*O + OH^- \rightarrow *OOH + e^-, \quad (3)$$

$$*OOH + OH^- \rightarrow * + O_2\ (g) + H_2O\ (l) + e^-, \quad (4)$$

where "*" represents the adsorption sites, which are generally the exposed metal sites.

The AEM free energy changes of each step can be calculated as:

$$\Delta G_1 = G(*OH) + 0.5\ G(H_2) - G(*) - G(H_2O) - eU, \quad (5)$$

$$\Delta G_2 = G(*O) + 0.5\ G(H_2) - G(*OH) - eU, \quad (6)$$

$$\Delta G_3 = G(*OOH) + 0.5\ G(H_2) - G(*O) - G(H_2O) - eU, \quad (7)$$

$$\Delta G_4 = G(*) + G(O_2) + 0.5\ G(H_2) - G(*OOH) - eU, \quad (8)$$

where U is the potential with respect to the normal hydrogen electrode (NHE).

The calculated overpotential (η) was then determined by:

$$\eta = \text{Max}\ [\Delta G_1, \Delta G_2, \Delta G_3, \Delta G_4] \quad (9)$$

The LOM pathway includes five steps, which are:

$$* O_a H + OH^- \rightarrow * O_a + H_2O (l) + e^-, \quad (10)$$

$$* O_a + OH^- \rightarrow * O_a OH + e^-, \quad (11)$$

$$* O_a OH + OH^- \rightarrow * O_a O + H_2O + e^-, \quad (12)$$

$$* O_a O \rightarrow * + O_2, \quad (13)$$

$$* + OH^- \rightarrow * O_a H + e^-, \quad (14)$$

where "*" represents the reaction sites. O_a denotes the activated lattice oxygen atoms.

The LOM free energy changes of each step can be calculated as:

$$\Delta G_1 = G(*O_a) + 0.5\ G(H_2) - G(*O_aH) - eU, \quad (15)$$

$$\Delta G_2 = G(*O_aOH) + 0.5\ G(H_2) - G(H_2O) - G(*O_a) - eU, \quad (16)$$

$$\Delta G_3 = G(*O_aO) + 0.5\ G(H_2) - G(*O_aOH) - eU, \quad (17)$$

$$\Delta G_4 = G(*) + G(O_2) - G(*O_aO), \quad (18)$$

$$\Delta G_5 = G(*O_aH) + 0.5\ G(H_2) - G(H_2O) - G(*) - eU, \quad (19)$$

The overpotential of LOM is calculated by:

$$\eta = \text{Max}\ [\Delta G_1, \Delta G_2, \Delta G_3, \Delta G_4, \Delta G_5] \quad (20)$$

The oxygen vacancy formation energy (Evac) of the high-entropy (oxy)hydroxide models was calculated by

$$\text{Evac} = E_{(\text{defective})} + 1/2E_{(O2,\ \text{corr})} - E_{(\text{perfect})}$$

where $E_{(\text{defective})}$ and $E_{(\text{perfect})}$ are the DFT energies for a bulk model with and without a defect (an oxygen vacancy), respectively. $E_{(O2,\ \text{corr})}$ is the corrected energy of a gas-phase triplet oxygen molecule after correction based on the experimental binding energy of oxygen (O_2).

1. Supplementary Figures

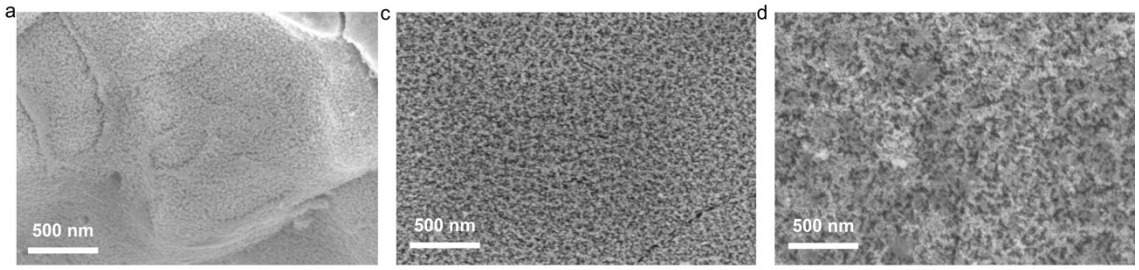

Figure S1 The SEM images of a) np-MnFeCoNiCu. b) np-MnFeCoNiAg. c) np-MnFeCoNiAu.

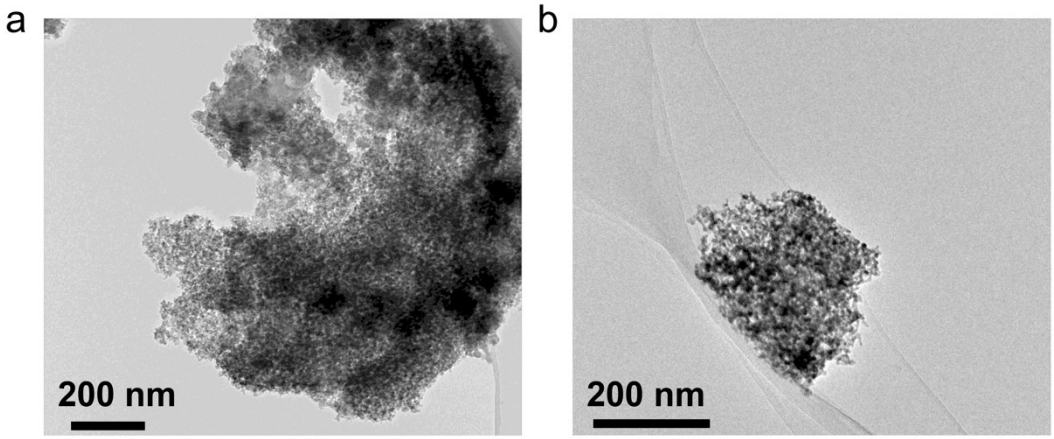

Figure S2 The TEM images of a) np-MnFeCoNiAg and b) np-MnFeCoNiAu.

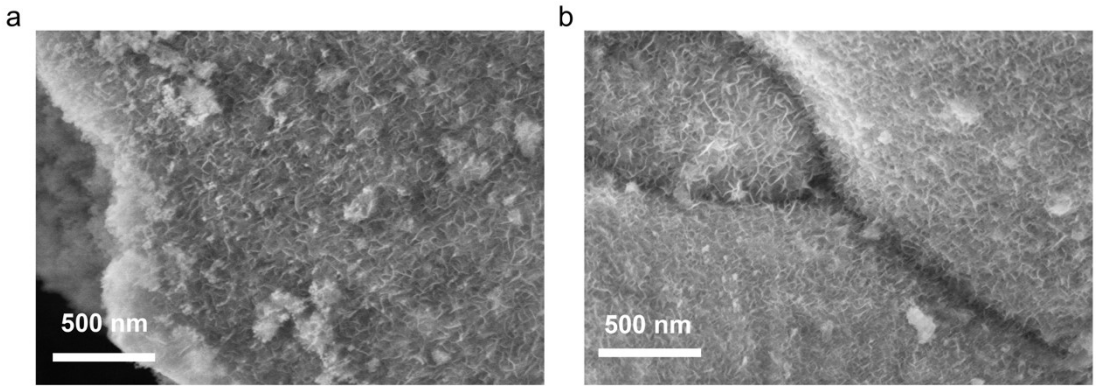

Figure S3 The SEM images of np-MnFeCoNiCuOOH

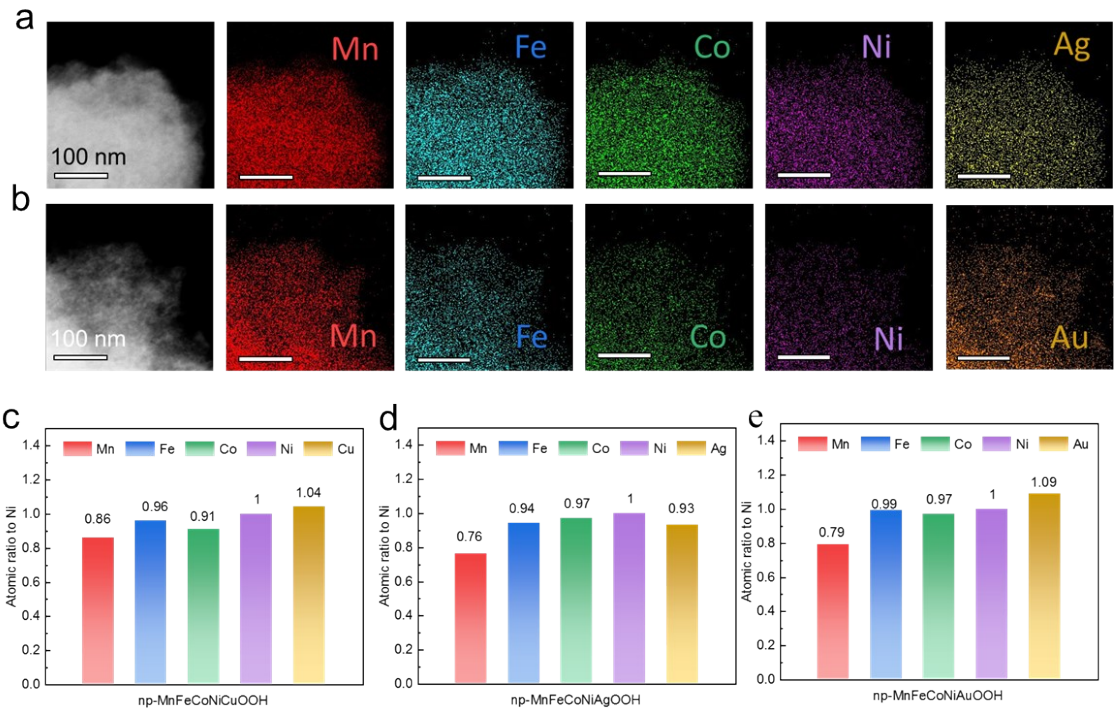

Figure S4 Elemental mapping of (a) np-MnFeCoNiAgOOH and (b) np-MnFeCoNiAuOOH. Atomic ratio to Ni of (c) np-MnFeCoNiCuOOH, (d) np-MnFeCoNiAgOOH and (e) np-MnFeCoNiAuOOH

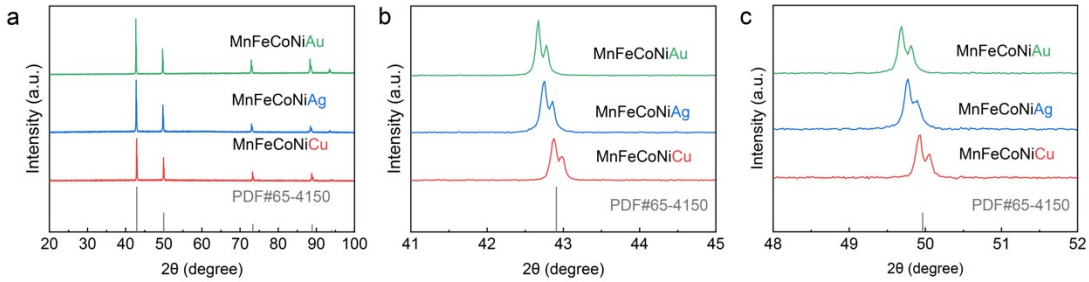

Figure S5 a) XRD spectra of the MnFeCoNiCu, MnFeCoNiAg and MnFeCoNiAu. b) the (111) plane XRD spectra of the MnFeCoNiCu, MnFeCoNiAg and MnFeCoNiAu. c) the (200) plane XRD spectra of the MnFeCoNiCu, MnFeCoNiAg and MnFeCoNiAu.

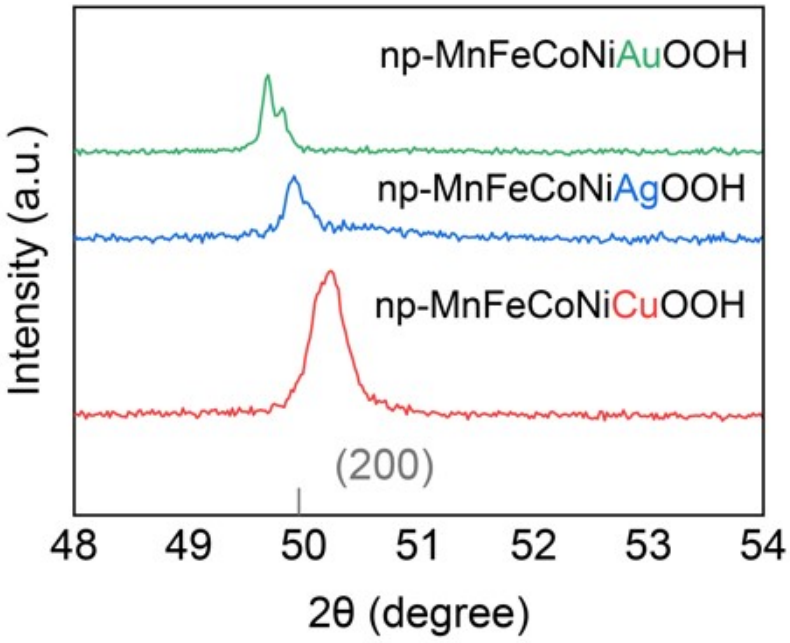

Figure S6 The (200) plane XRD spectra of the MnFeCoNiCu, MnFeCoNiAg and MnFeCoNiAu.

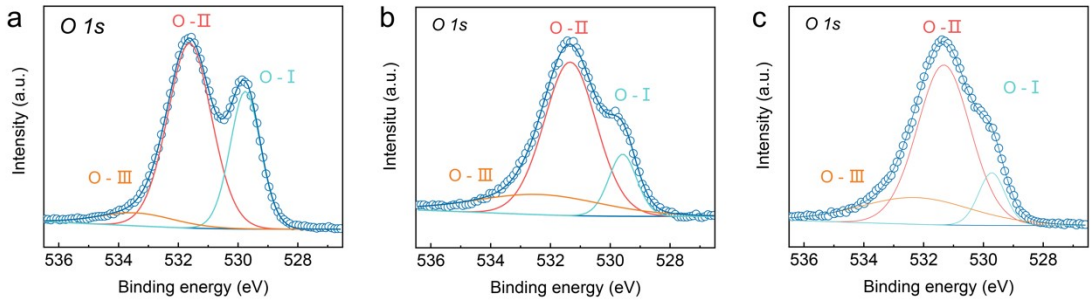

Figure S7 XPS spectra od O 1s in a) np-MnFeCoNiCuOOH, b) np-MnFeCoNiAgOOH and c) np-MnFeCoNiAuOOH

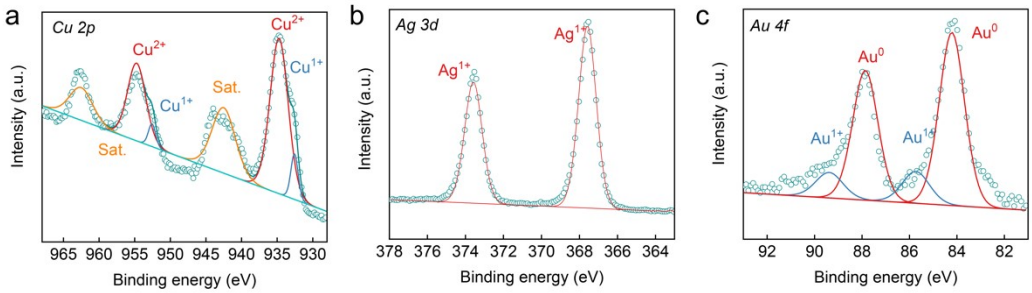

Figure S8 XPS spectra of a) Cu 2p in np-MnFeCoNiCuOOH, b) Ag 3d in np-MnFeCoNiAgOOH and c) Au 4f in np-MnFeCoNiAuOOH

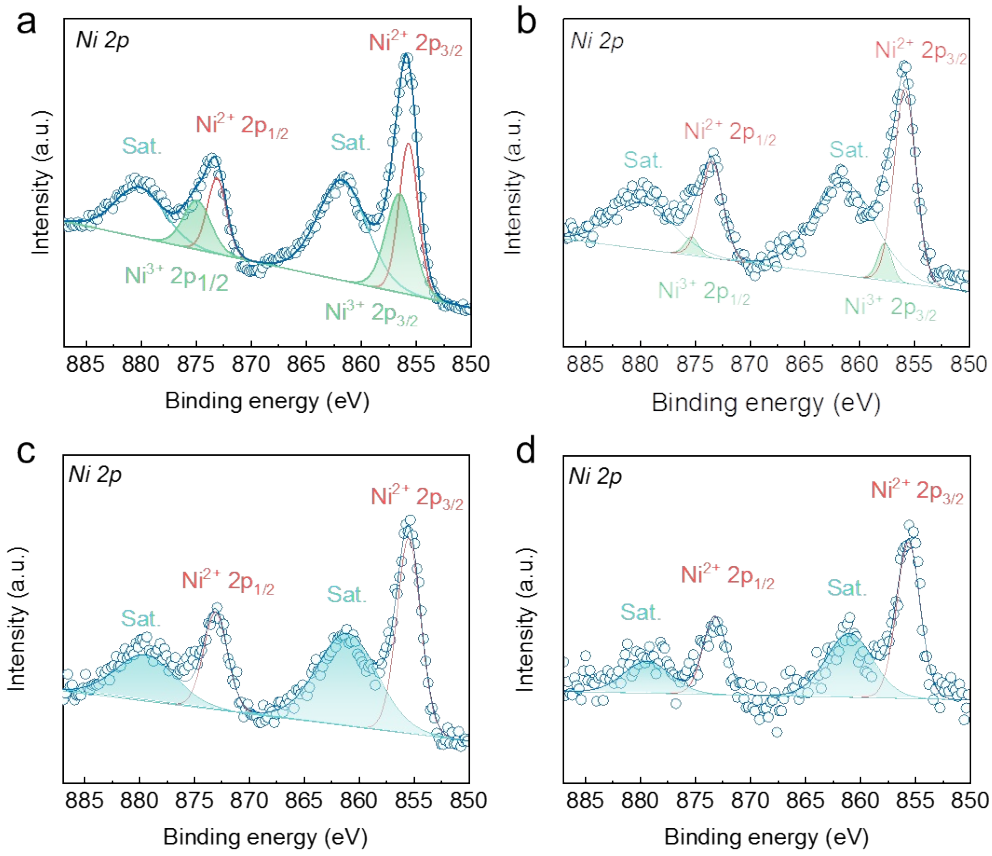

Figure S9 XPS spectra of Ni 2p in (a) np-MnFeCoNiOOH, (b) np-MnFeCoNiCuOOH and (c) np-MnFeCoNiAgOOH and (d) np-MnFeCoNiAuOOH

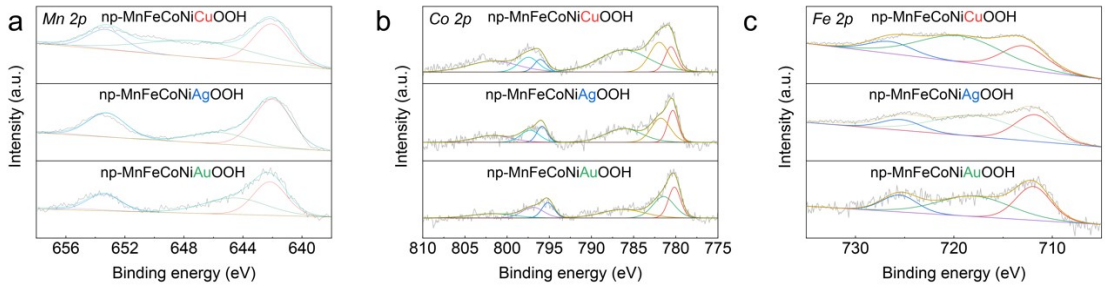

Figure S10 XPS spectra of (a) Mn 2p, (b) Co 2p and (c) Fe 2p in MnFeCoNiCuOOH, MnFeCoNiAgOOH and MnFeCoNiAuOOH.

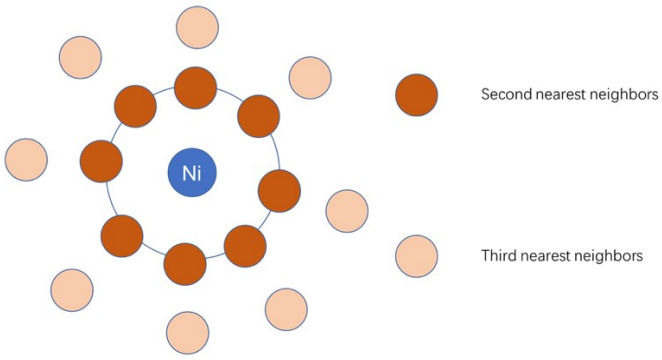

Figure S11 Nearest neighbors' principle.

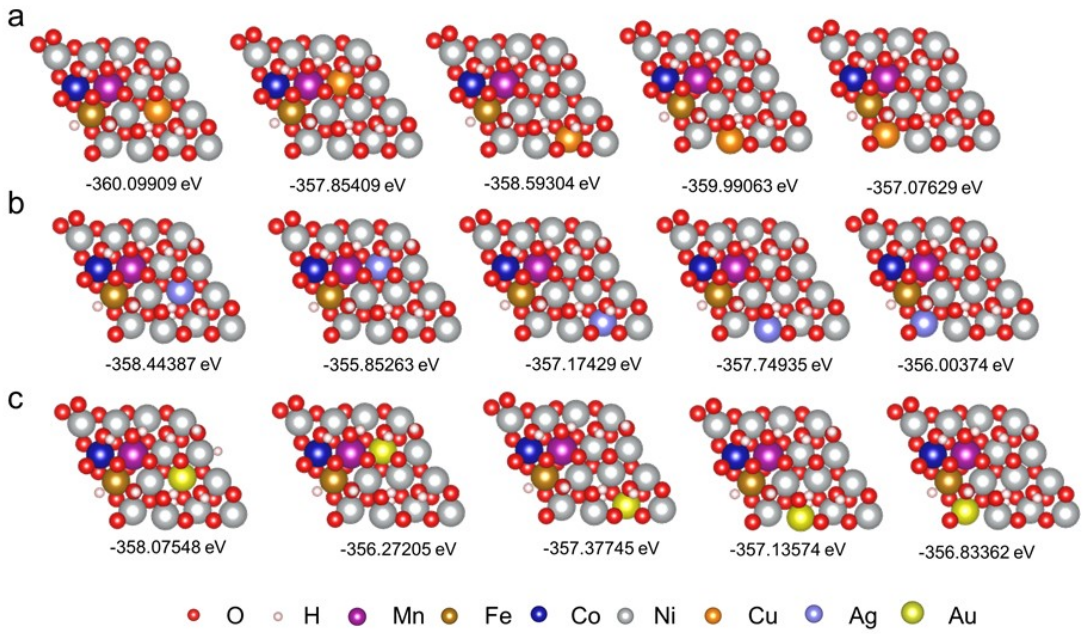

Figure S12 Energy of a) MnFeCoNiCuOOH, b) MnFeCoNiAgOOH and c) MnFeCoNiAuOOH

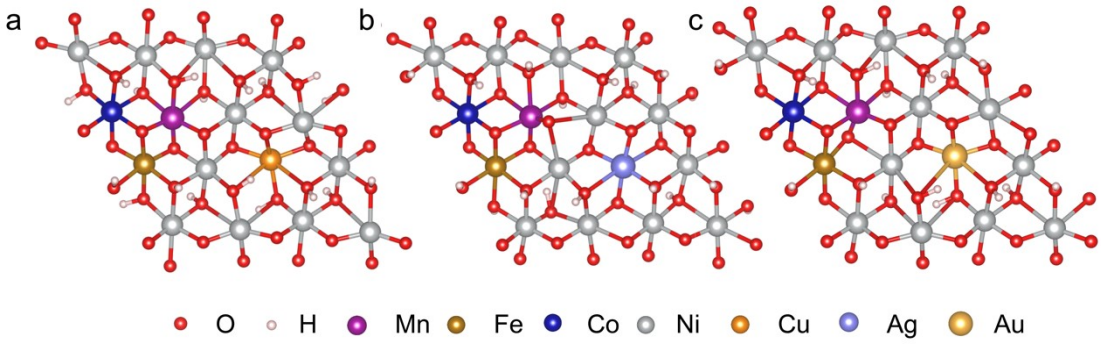

Figure S13 Calculation model for (a) MnFeCoNiCuOOHOOH, (b) MnFeCoNiAgOOHOOH and (c) MnFeCoNiAuOOHOOH.

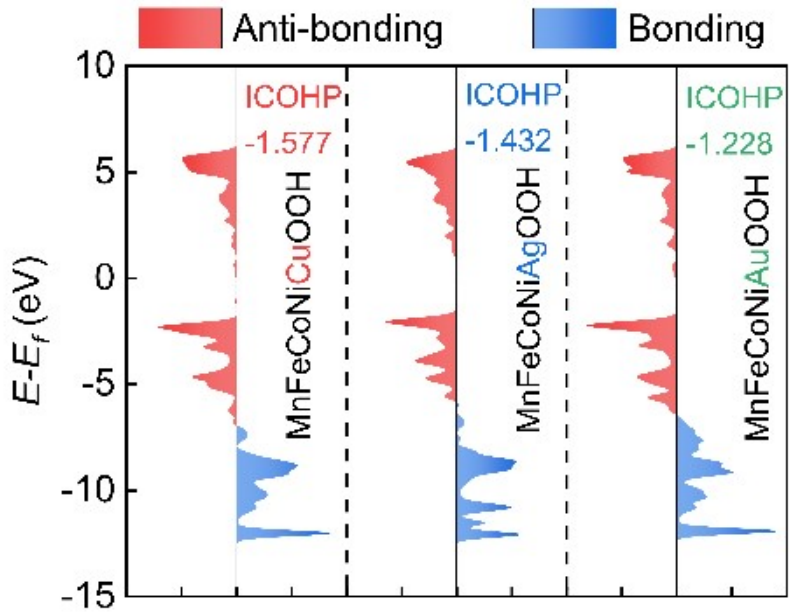

Figure S14 Crystal orbital Hamiton populations (COHP) of Ni-O in electrocatalysts

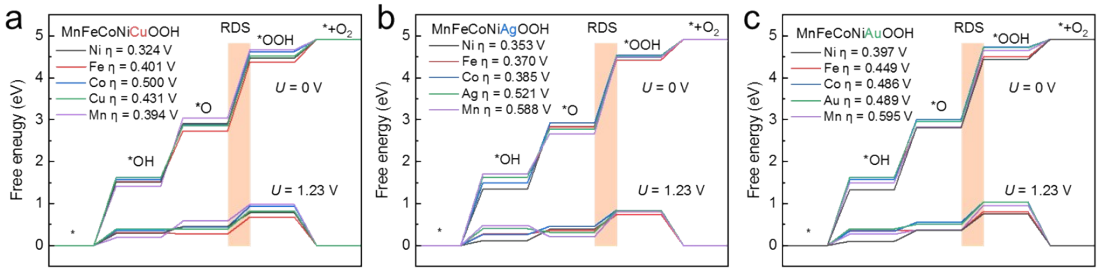

Figure S15 AEM on (a) MnFeCoNiCuOOH, (b) MnFeCoNiAgOOH and (c) MnFeCoNiAuOOH surface at a potential of 0 V.

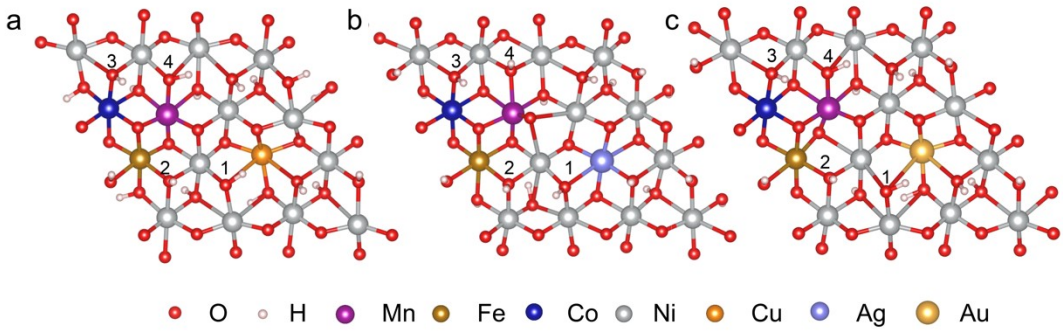

Figure S16 Different adsorption sites for (a) MnFeCoNiCuOOH, (b)MnFeCoNiAgOOH and (c)MnFeCoNiAuOOH.

During the theoretical calculations, in the all electrodes, 1, 2, 3 and 4 as the active centers for the LOM pathway active centers.

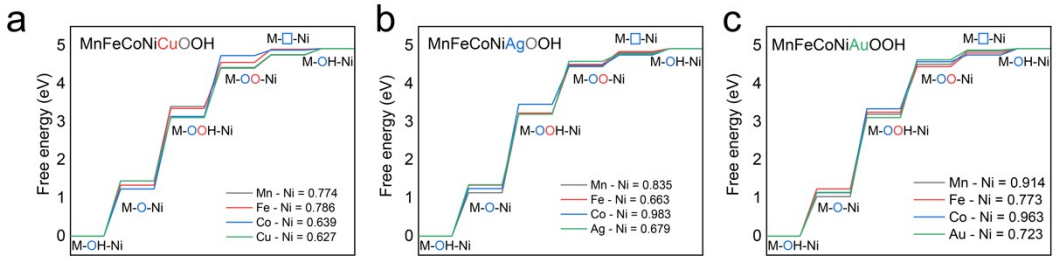

Figure S17 LOM on (a) MnFeCoNiCuOOH, (b)MnFeCoNiAgOOH and (c) MnFeCoNiAuOOH surface at a potential of 0 V.

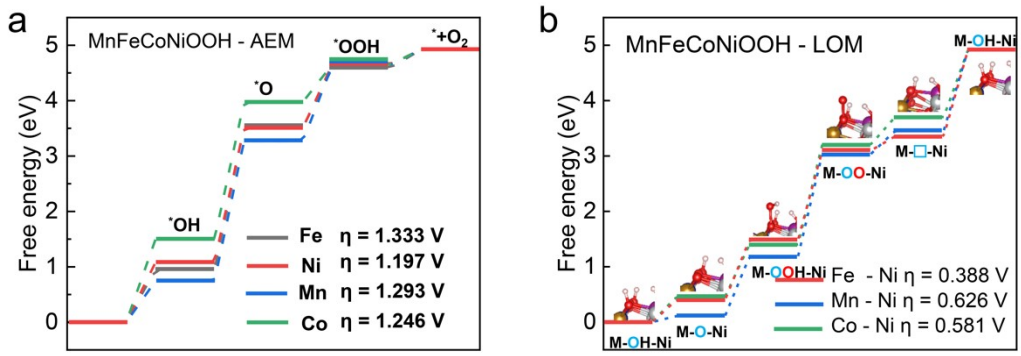

Figure S18 (a) AEM and (b) LOM on MnFeCoNiOOH surface at a potential of 0 V.

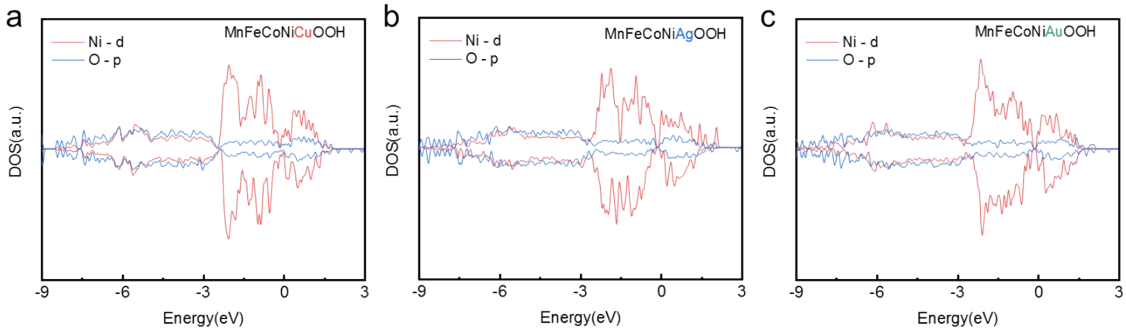

Figure S19 Density of state (DOS) of electrocatalysts a) MnFeCoNiCuOOH, b) MnFeCoNiAgOOH and c) MnFeCoNiAuOOH.

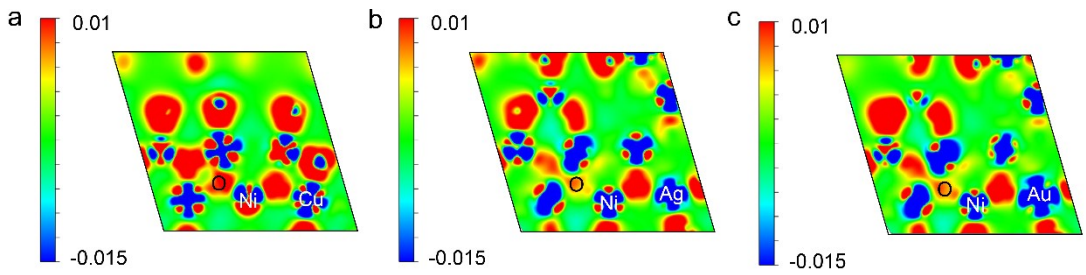

Figure S20 Differential charge density for **a**) MnFeCoNiCuOOH, **b**) MnFeCoNiAgOOH and **c**) MnFeCoNiAuOOH

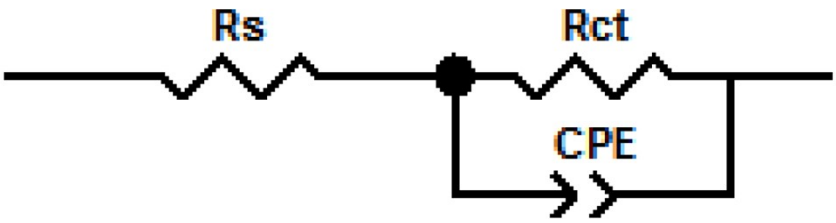

Figure S21 Equivalent circuit simulations.

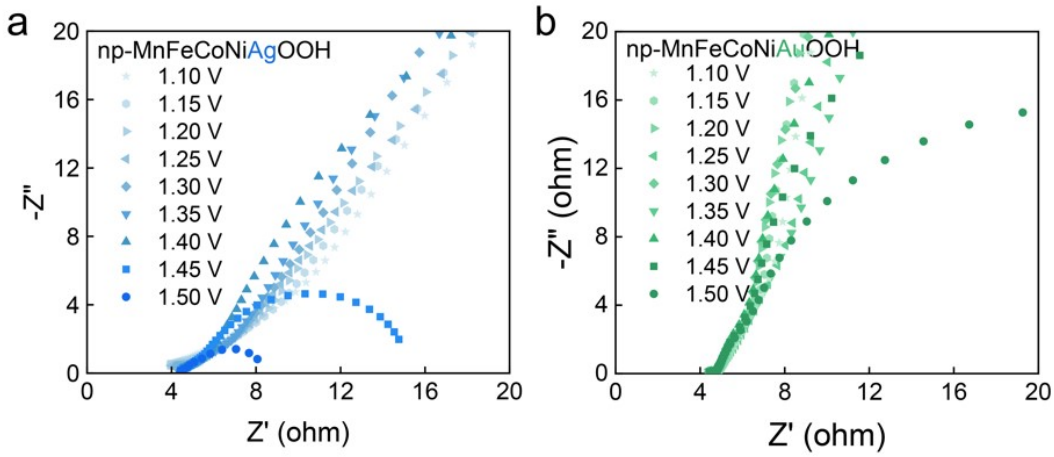

Figure S22 The resistance of the activated composite electrodes under different applied potentials

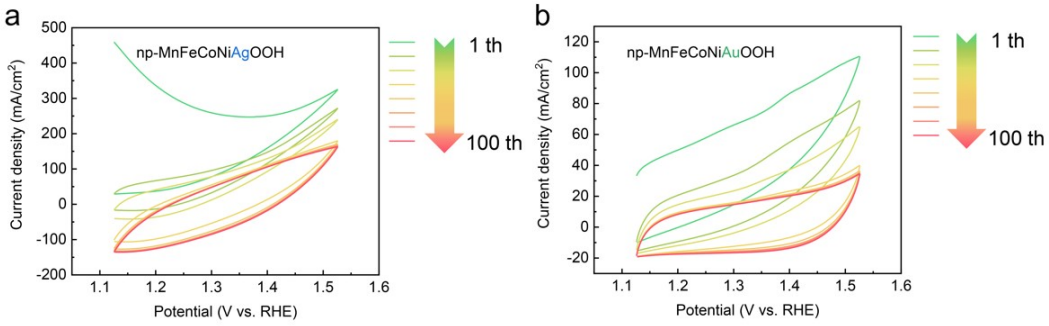

Figure S23 CV electrochemical activation process curve of (a) np-MnFeCoNiAgOOH and (b) np-MnFeCoNiAuOOH at the 100 mV/s from 0.2 V to 0.6 V vs. Hg/HgO.

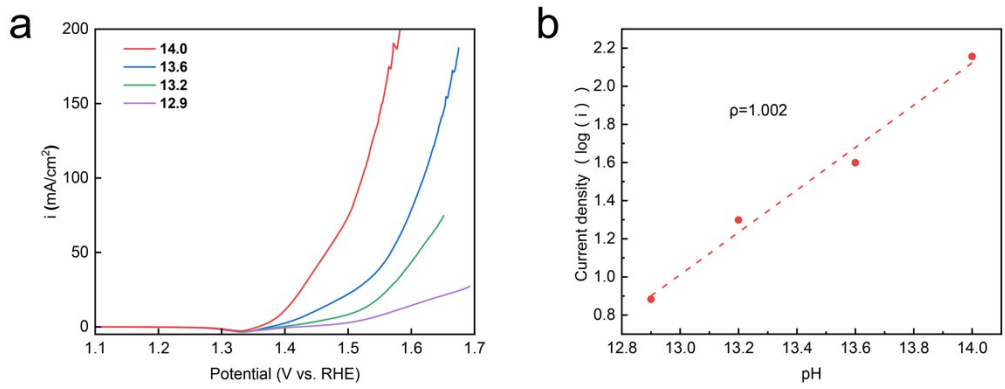

Figure S24 (a) LSV curves for np-MnFeCoNiOOH electrocatalyst measured in KOH with pH = 12.9, 13.2, 13.6 and 14.0. (b) OER current density at 1.55 V vs. RHE drew in log scale as a function of pH, from which dependency relationship ($\rho = d\log i/d\mathrm{pH}$) between the catalytic performance of different catalysts and the pH were calculated.

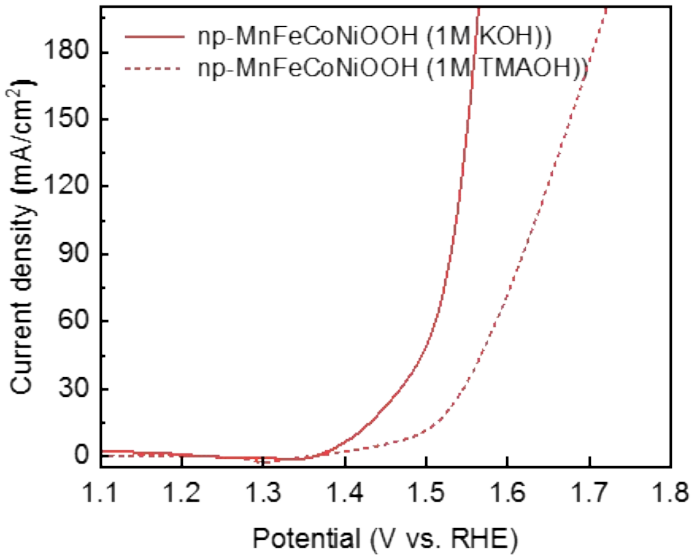

Figure S25 LSV curves for np-MnFeCoNiOOH electrocatalyst measured in 1 M KOH and 1 M TMAOH.

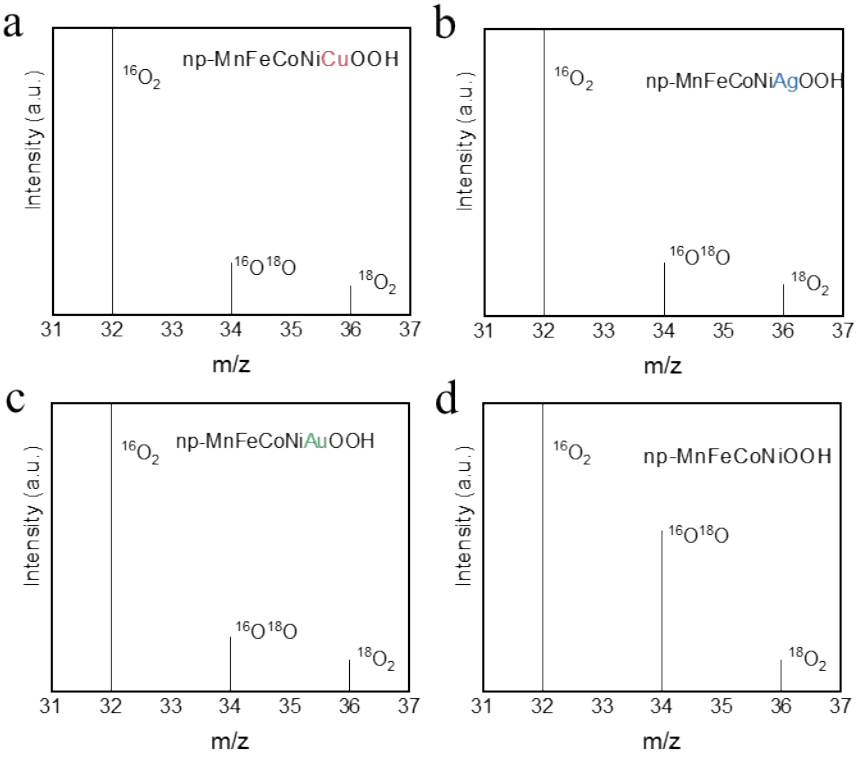

Figure S26 The detected MS signals of generated oxygen molecule using $^{16}O^{18}O$ isotope-labeled.

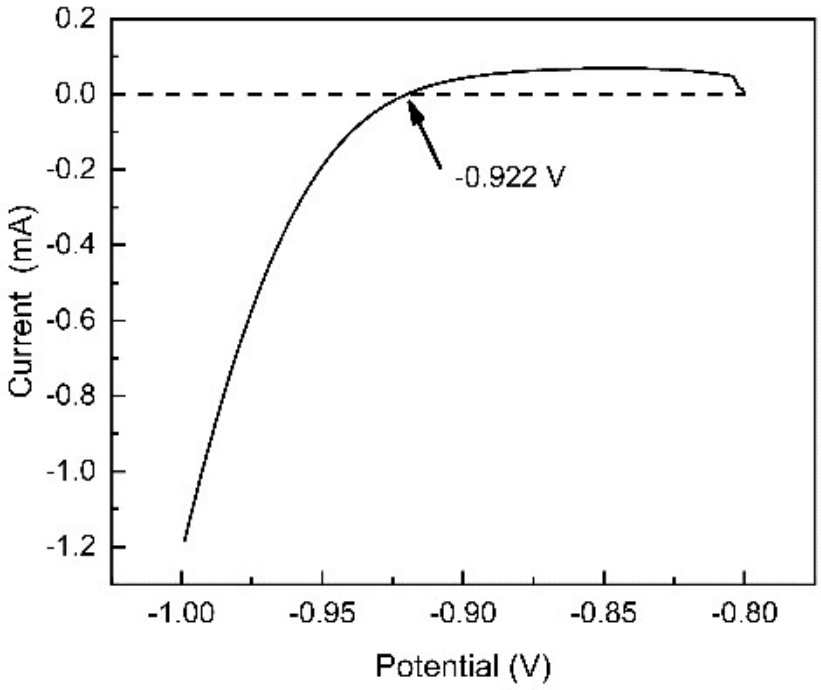

Figure S27 LSV curves for cleaned platinum sheets in H_2-saturated electrode.

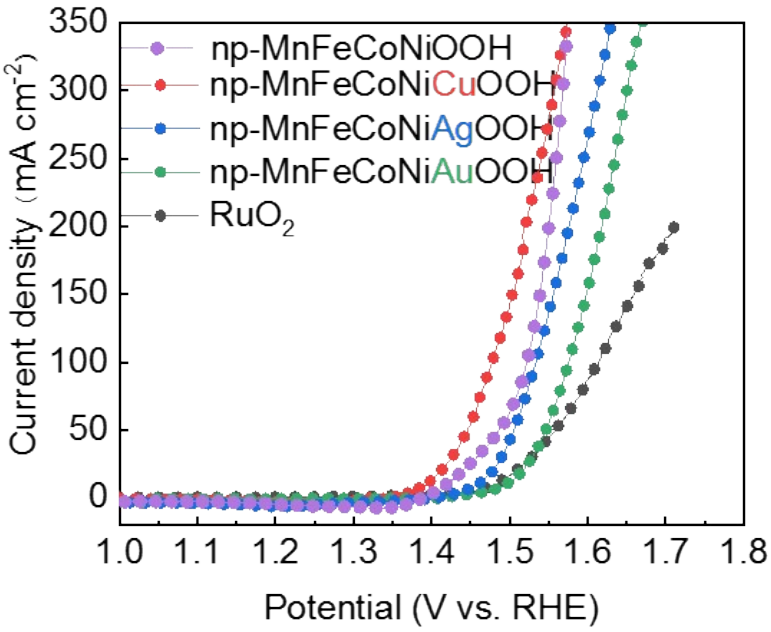

Figure S28 OER linear sweep voltammetry (LSV) of np-MnFeCoNiOOH, np-MnFeCoNiCuOOH, np-MnFeCoNiAgOOH and np-MnFeCoNiAuOOH electrocatalyst.

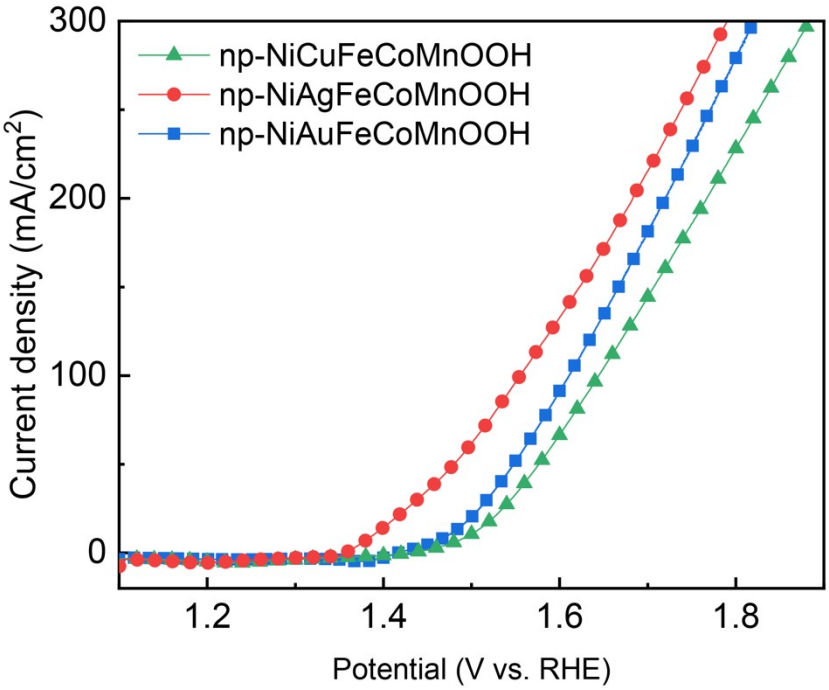

Figure S29 LSV curves of np-MnFeCoNiCuOOH, np-MnFeCoNiAgOOH and np-MnFeCoNiAuOOH without iR-corrected.

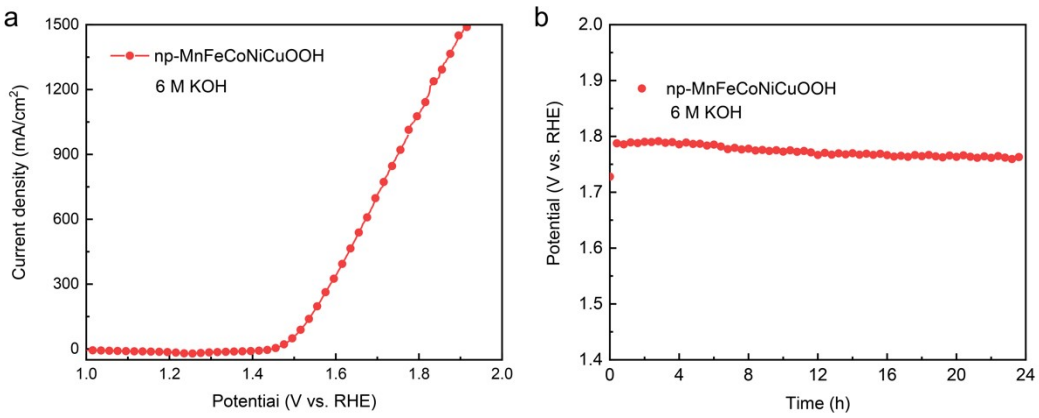

Figure S30 (a) LSV and (b) Cp (1000 mA/cm$_2$) test of MnFeCoNiCuOOH in 6 M KOH.

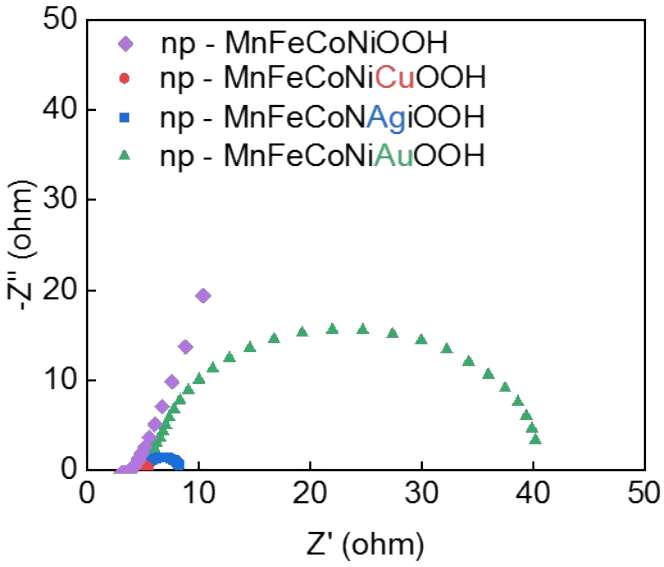

Figure S31 EIS spectra of of np-MnFeCoNiOOH, np-MnFeCoNiCuOOH, np-MnFeCoNiAgOOH and np-MnFeCoNiAuOOH electrocatalyst.

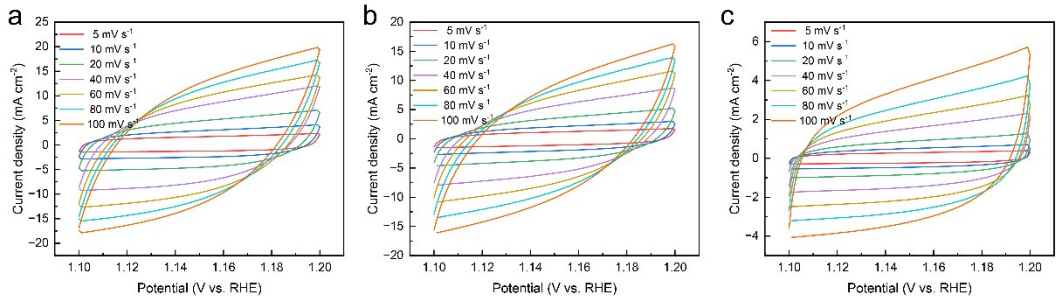

Figure S32 Double-layer capacitance (C_{dl}) of (a) np-MnFeCoNiCuOOH, (b) np-MnFeCoNiAgOOH and (c) np-MnFeCoNiAuOOH

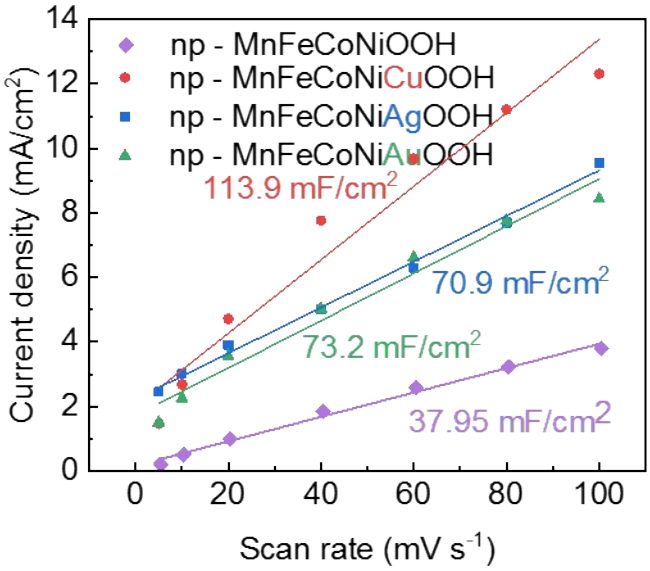

Figure S33 Double-layer capacitances (C_{dl}) of of np-MnFeCoNiOOH, np-MnFeCoNiCuOOH, np-MnFeCoNiAgOOH and np-MnFeCoNiAuOOH electrocatalyst.

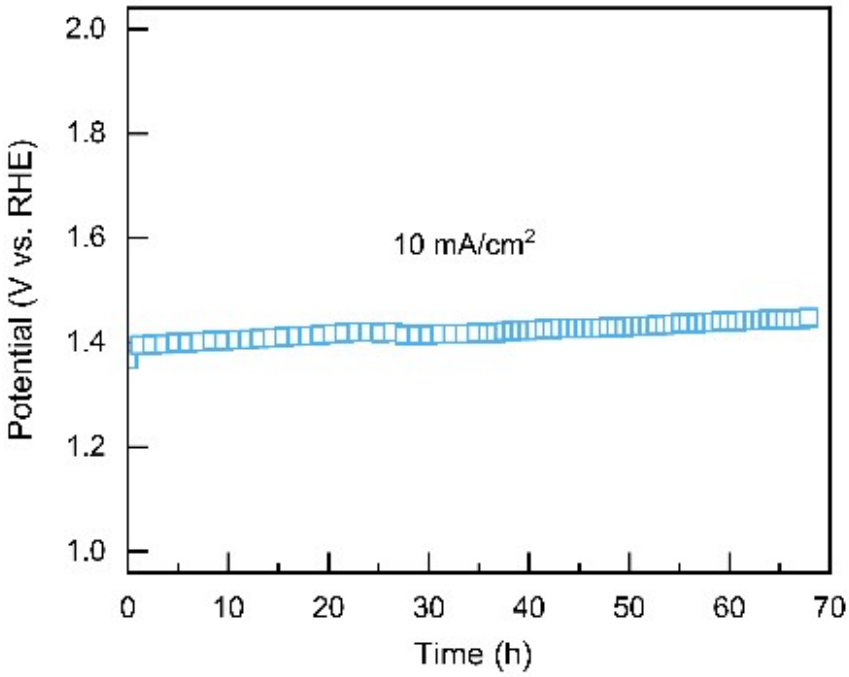

Figure S34 CP (10 mA/cm^2) test of np-MnFeCoNiOOH electrocatalyst

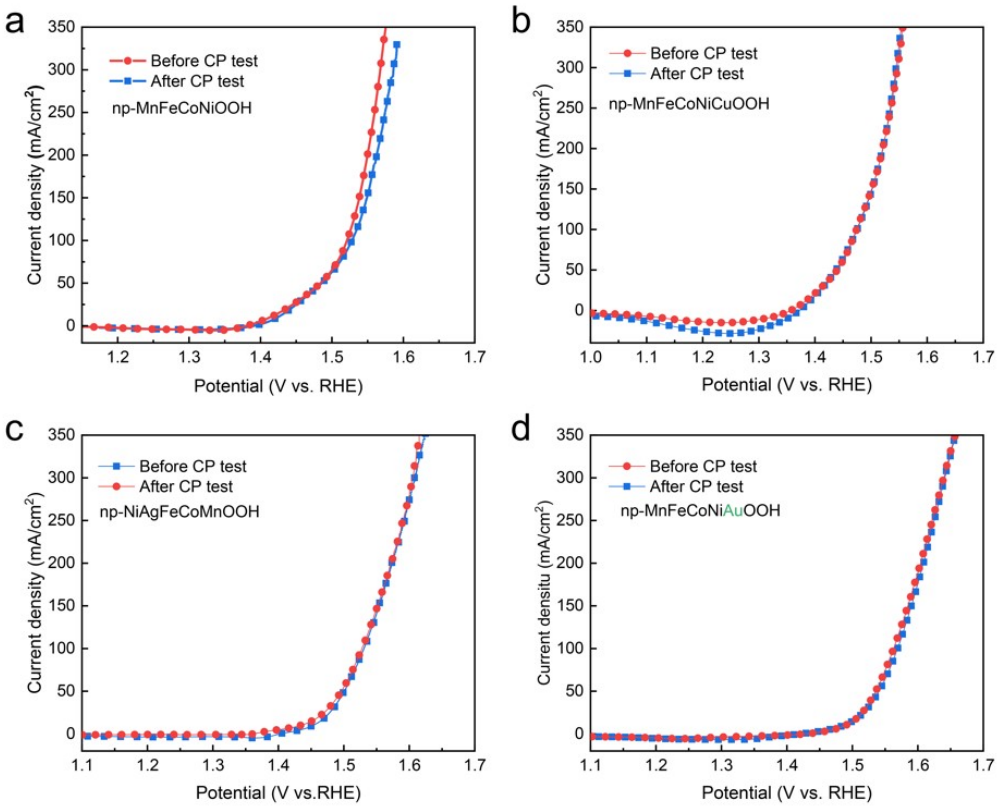

Figure S35 LSV curves of np-MnFeCoNiOOH, np-MnFeCoNiCuOOH, np-MnFeCoNiAgOOH and np-MnFeCoNiAuOOH after CP test.

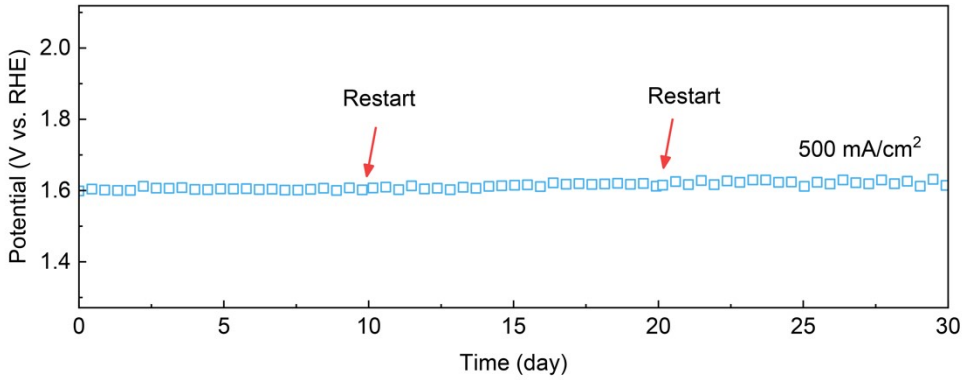

Figure S36 CP (500 mA/cm^2) test of np-MnFeCoNiCuOOH electrocatalyst.

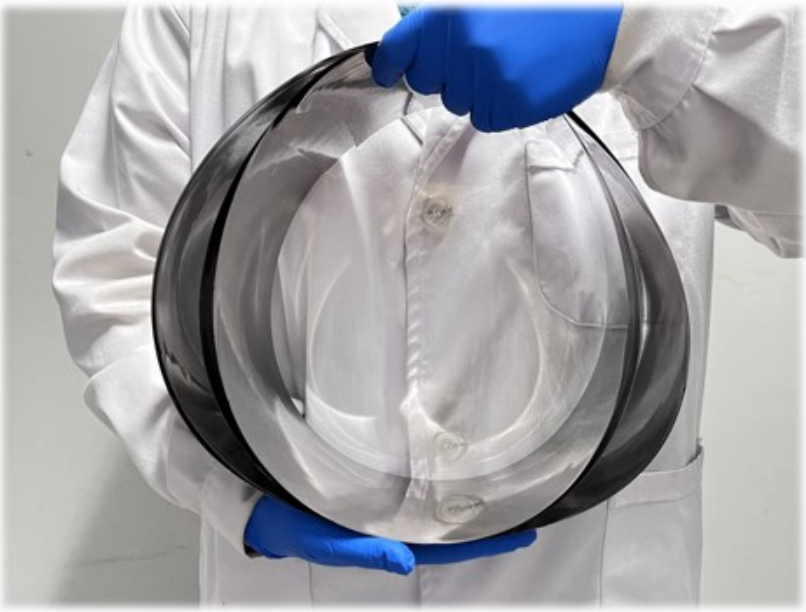

Figure S37 Macroscopic photographs of the square meter-sized electrocatalysts.

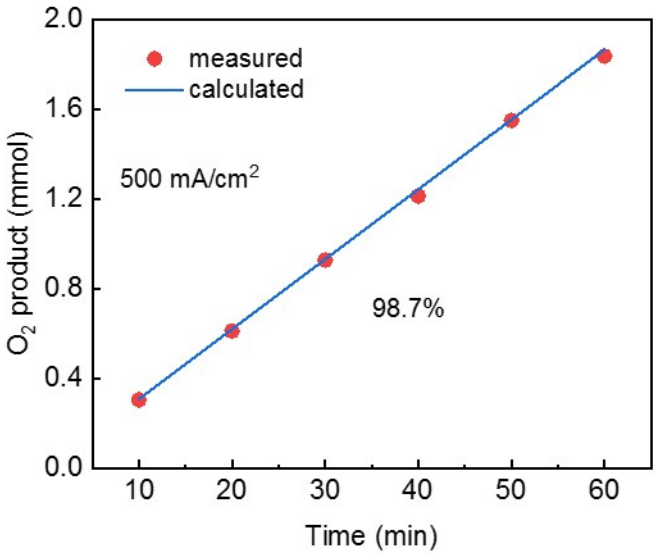

Figure S38 Faradaic efficiency of np-MnFeCoNiCuOOH at 500 mA/cm^2.

Table 1 The detected MS results of generated oxygen molecule using $^{16}O^{18}O$ isotope-labeled

	$^{16}O^{16}O$(ppm)	$^{16}O^{18}O$(ppm)
np-MnFeCoNiCuOOH	242399.10	1014.99
np-MnFeCoNiAgOOH	229161.37	959.44
np-MnFeCoNiAuOOH	232467.53	973.33
np-MnFeCoNiOOH	237494.36	8832.72
natural abundance	218118.18	913.25

Table 2 The Rate of degradation for voltage before and after the CP

	Rate of degradation
np-MnFeCoNiOOH	12.76%
np-MnFeCoNiCuOOH	0.32%
np-MnFeCoNiAgOOH	0.25%
np-MnFeCoNiAuOOH	0.26%

Table 3 The detected ICP-MS result

Element	Content(μg/L)
Mn	4.1
Fe	9.8
Co	0.1
Ni	1.9
Cu	176.1